Contents lists available at http://qu.edu.iq

Al-Qadisiyah Journal for Engineering Sciences

Journal homepage: https://qjes.qu.edu.iq

Experimental Evaluation of Polyurethane Capsule Placement in Hollow Brick Walls for Optimized Thermal Insulation Under hot-climate Conditions

Mohammad Yaseen Shaker [1] *, Hayder M. Abbas [1]

[1] *Department of Mechanical Engineering, College of Engineering, University of Al-Qadisiyah, Al-Qadisiyah 58001, Iraq*

ARTICLEINFO

Article history:
Received
Received in revised
Accepted

Keywords:
Thermal insulation
Optimal location
Heat flux
Polyurethane capsules
Hollow brick wall

ABSTRACT

This paper presents an experimental study of the effects of polyurethane (PU) capsule position on heat gain in hollow brick walls in real outdoor environments. The experiments were carried out in October 2024 at the University of Al-Qadisiyah, Middle Area Desert, Al-Diwaniyah, Iraq, during an ambient temperature range from 22 to 39 °C and peak solar radiation intensities of (750 W/m²) (horizontally) and [650W/m²] (south-facing vertical). Two identical cubic test cells (1 m × 1 m × 1 m) were built and thermally calibrated to have identical baselines. Two wall configurations were tested: PU capsules in the outer cavity row (external) and in the inner cavity row (internal). The results demonstrate the superior thermal insulation capacity of the outboard position. The maximum surface temperature of the outer wall in the externally insulated condition was 46.7 °C, compared with 45.4 °C for the inner wall, indicating better heat interception by the outer exposed layer (exterior). Internal surface temperatures were 36.0 °C and 37.2 °C at the external and internal positions, respectively (less heat transfer). Indoor ambient temperatures were 33.8 °C with external installation and 34.3 °C with internal installation. The peak heat flux rate on the south wall decreased from 72.2 W/m² (internal) to 58.7 W/m² (external), a 19% decline. These findings apparently demonstrate that if PU capsules are placed in the outer cavity row of hollow brick walls, solar heat can be intercepted successfully before entering the wall mass, thereby improving thermal resistance and reducing cooling requirements for hot-climate buildings.

1. Introduction

Energy use in the building sector is one of the most significant contributors to global energy consumption, with heating and cooling systems accounting for about 40-50% of building energy use [1]. Comfortable indoor temperatures with minimal cooling loads are becoming increasingly important, especially in hot-climate areas, due to rising energy costs and environmental impacts. Thermal insulation prevents heat transfer between building envelopes, resulting in energy savings and higher comfort for building users.

Many researchers have investigated insulated materials and methods to develop new insulation materials that enhance building envelope performance. For example, in a case study examining the sustainability of polyurethane (PU) insulation, Kotaji and Loebel [2]. Completely insulated walls were assessed using life cycle assessment (LCA) and life cycle costing (LCC), and a low thermal conductivity of 0.022 W/m.K was identified for PU insulation, leading to a 43-57% reduction in global warming potential. In addition, Tangjuank [3] reported an experimental

* *Corresponding author.*
E-mail address: mohammadshaker@qu.edu.iq (Mohammad Yaseen Shaker)

https://doi.org/10.30772/qjes.00000.0000

Nomenclature:

A	Area, m²
Cp	Specific heat capacity, J/(kg·K)
h	Convective heat transfer coefficient, W/(m²·K)
hfg	Latent heat of fusion of ice, kJ/kg
I	Solar radiation intensity, W/m²
k	Thermal conductivity, W/(m·K)
L	Thickness, m
m	Mass, kg
q	Heat flux, W/m²
Q	Heat transfer rate, W
R	Thermal resistance, m²·K/W
T	Temperature, °C
U	Overall heat transfer coefficient, W/(m²·K)
x	Distance in direction of heat flow, m

Greek symbols

ε	Surface emissivity
σ	Stefan-Boltzmann constant, W/(m²·K⁴)
σ_{total}	Total uncertainty
σ_{sensor}	Sensor uncertainty
$\sigma_{instrument}$	Instrument uncertainty
ΔT	Temperature difference, °C

Subscripts

amb	Ambient
cond	Conduction
conv	Convection
E	East room/wall
ext	External surface
int	Internal surface
rad	Radiation
total	Total value
W	West room/wall

investigation on the thermal insulation characteristics of pineapple leaves based on particleboards. Using ASTM testing, it was observed that the particleboards had a thermal conductivity of 0.035 W/m·K and a density of 210kg/m³, and could therefore replace traditional synthetic insulators. Similarly, Al-Mogbel et al. [4] conducted a numerical study on the insulation performance of building elements in Saudi Arabia. Employing air-dynamic calculations and HAP software for 1022 variants revealed that the roof is the most thermally loaded, accounting for 44.2% of the total heat load, and that a single wall of cement-polyurethane should be preferred.

Meng et al. [5] conducted a numerical investigation to assess the wall thermal transmittance using the Simple Hot Box-Heat Flow Meter (SHB-HFM) method. To this end, they performed numerical simulations that showed that increasing the temperature difference from 10°C to 30°C reduced the system error by 4.4%-7.5%, and they derived a fit formula to determine the minimum dimension of the hot box. Castleton, Stovin et al. [6] reviewed the literature to determine green roofs' energy-saving potential. Analyzing data from other researchers and thermal simulation software demonstrated that a green roof can decrease heat gain by 70-90% in summer and heat loss by10-30% in winter, providing 2% to 44% energy savings. Waheb [7] conducted an experimental study to investigate the extent to which insulation reduced cooling loads in Iraqi buildings. Thermometer sensors and solar power meters showed that adequate insulation could cut annual cooling energy use by 65 kWh/m² (i.e., 30 per cent savings).

Additionally, Chihab, Garoum et al. [8] numerically analyzed the dynamic thermal behavior of multilayer hollow clay brick walls. Using a finite element method simulation of the Navier-Stokes and energy equations, the authors observed that when insulation was installed in the cavities, the peak temperature was delayed by 2.3 hours and the total thermal load was reduced by 28%. Huang et al. [9] performed additional experimental research to optimize the insulation performance of composite self-insulating hollow blocks. They tested performance in the hollow-block shrouds using cold- and hot-box tests. They found that the insulation effect of EPS-filled hollow blocks improves, and that the higher the filling rate, the better the insulation effect.

Meng et al. [5] studied the thermal behavior of sintered hollow bricks inserted into EPS insulation. Furthermore, Zukowski and Haese [10] experimentally and numerically studied the thermal performance of a hollow brick containing perlite insulation. They used the calibrated hot-box apparatus and the finite-volume method to determine the heat capacity to be 855.1 J/(kg·K) and the thermal conductivity to be 0.09 W/(m·K) for brick. Additionally, Hashim [11] experimentally evaluated the applicability of an Iraqi passive house in the summer. They concluded that a reduction of up to 30 °C in indoor temperature and an 80% reduction in cooling energy use can be achieved using the passive house model and a Lutron data logger. Nagy et al. [12] investigated the hygrothermal behavior of masonry blocks with various thermal insulation materials. Through finite element simulations, the work showed a 31% improvement in the thermal performance of polyurethane foam compared to perlite, and the manufacturer's deviation due to separation markedly influenced thermal transmittance. Ali et al. [13] developed a numerical simulation approach to investigate the thermal performance of Egyptian perforated red brick masonry. Using a finite-volume model and a FORTRAN code, they determined that the equivalent thermal conductivity decreased by almost 45% when cavities in these materials were filled with polyurethane foam or cork, thereby increasing thermal resistance. Jerman et al. [14] experimentally investigated hollow bricks which were filled separately. They reported the lowest thermal conductivity of hydrophilic mineral wool, 0.074 W/(m·K), in a steady-state experiment conducted in two climate chambers with air-filled cavities, yielding the worst outcome.

In addition, Hashim [11] made a numerical analysis of the thermal insulation of red clay bricks. The method they have employed is the ABAQUS finite element. According to their report, the hollow brick cemented with PUF can significantly reduce thermal conductance due to convection and radiation in the air-filled inter-hollow spaces of the brick. Al-Homoud [15] developed a simulation to assess the performance of thermal insulation in buildings of different types and climates, specifically in hot climates. The research conducted using the EnerWin hourly building energy simulation tool showed that the edifice could save 37% and 28% of energy annually in Riyadh and Jeddah, respectively. In addition, Abdulsada et al. [9] examined the impact of effective pebble insulation on the thermal properties of the construction members in hot, dry climates. They applied

their technique to two building models in Kirkuk, Iraq, and implemented a local computer simulation model based on ASHRAE relationships, finding that the cooling load energy was reduced by 70%. Knez et al. [16] explored the processes of recycling waste polyurethane foam (PUR) as a building envelope material of geopolymer. They found that incorporating PUR into the geopolymer reduced the composite density to 1.6 kg/L and improved thermal insulation by 10%, as determined using several analytical techniques. Prajapati [17] studied the research on building insulation. They applied three insulating materials and a K-type thermocouple and detected a temperature difference of 5.5 ℃ between a model that consisted of aerogel, hempcrete, and wooden ware/pulp and the other materials. Another experimental investigation conducted by Zhang et al. [18] was performed to develop the heat-insulating performance of agricultural waste hollow bricks. It was indicated that for the species of HF-1-B-type heat-flow meter, the insulating properties of rice straw-filled hollow bricks reduced the whole heat transfer coefficient, amounting to 32.7% lower than those in bare specimens (1.59 W/(K·m²) and 1.07 W/(K·m²). Another report by Merli [19] studied in detail the thermal performance of 15 load-bearing and infill wall configurations with different cavity-filling materials. Experimental results confirmed that both expanded polystyrene (EPS) blobs and graphitized EPS dribbles significantly improved the thermal performance of brick assemblies. Quantitative analysis conducted in this research demonstrated that these new filling materials could decrease the equivalent thermal conductivities by 4-12%, demonstrating the potential of EPS-based fillers as practical media for improving the thermal insulation performance of masonry construction elements.

The latest trends in building-envelope insulation reinforce the effectiveness of self-insulating building envelopes, where optimising cavity fillings significantly improve wall thermal performance and reduces heat transfer without increasing wall thickness or construction complexity [20-23]. Other walls with hollow clay and concrete walls that embrace full cavity insulation are found to reach similar conclusions on the thermal performance gains which promote the dynamic performance, as more thermal time lag and decadent factors cause the heating and cooling loads to be smaller, in comparison under climatic conditions varying [8, 24-26]. Other energy efficiency measures include walls, roofs, and composite envelopes with phase change material that offers latent heat storage, even out indoor temperature variations, and delay heat transfer. It is also highly dependent on the PCM phase-change temperature, location, and thickness [27-31]. Simultaneously, research shows that optimizing the internal air-cavity geometry can maximize insulation performance by reducing conductive and convective heat transfer while retaining structural performance [8, 32]. Bio-derived products, waste products, and insulations, e.g., agricultural fibres and recycled construction waste, have proven to be sustainable insulations due to their ability to regulate thermal conductivity, stabilise indoor environments, and support low-carbon construction objectives [33, 34]. More recently, concepts of hybrid envelopes, which involve traditional insulation combined with green walls/energy-active covers, have demonstrated the potential to provide greater thermal buffering and passive comfort but are weather-dependent, retrofit design-dependent, and constrained by financial limits [26, 35].

Existing studies on thermal insulation for hollow brick walls have predominantly employed numerical modelling or laboratory-based testing, which do not capture the transient thermal behaviour imposed by real climatic conditions. Consequently, the optimal positioning of insulation within brick cavities remains experimentally unresolved. This work introduces a novel field-based experimental methodology in which two thermally calibrated test rooms, differing solely in polyurethane capsule placement external versus internal cavity row, were simultaneously exposed to solar radiation under hot-climate conditions in Al-Diwaniyah, Iraq. Heat flux, inner-surface temperature, and indoor air temperature were carefully measured to find the best insulation arrangement. This study helps theoretical and practical work come closer together by experimentally confirming the optimal placement of insulation in hollow brick walls under real outdoor conditions.

2. Methodology

2.1 Test Model Description

This prototype device was designed and produced in the College of Engineering, Research Zone of the University of Al Qadisiyah. This model was developed to study heat transfer in building walls, and it includes encapsulated polyurethane foam PUF used to fill the hollow sections in brick walls in typical weather conditions. The same experimental setup includes two identical cubic test chambers, which can test thermal performance under very well-controlled conditions, and a small container between them that contains the measuring devices. Both chambers are rectangular, 1 m deep, 1 m wide, and 1 m high. This provides a common testing ground for comparison.

Sandwiched is the construction of walls and floor systems for each chamber. These panels consist of a polyurethane core enclosed between layers of white polystyrene 0.02 m thick on the outsides (external side and inside), as shown in Fig. 1. The construction of the roof assembly can be similar. However, by adding a 0.05 m-thick external polystyrene layer, the system's overall thermal insulation performance is dramatically increased.

The roof assembly adds a further 0.05 m-thick polystyrene layer (same material properties as the wall insulation, k = 0.035 W/(m·K) to compensate for the higher solar radiation intensity on horizontal surfaces, which can reach 750 W/m^2 at solar noon. This improved roof insulation ensures that the main heat path lies through the south-facing test wall, allowing both insulation configurations to be compared for an accurate assessment.

Two effective wall geometries are designed for each chamber supporting the test protocol. There is a square aperture (0.5 × 0.5 m internally) cut into the south wall of the shack, which has been framed and celled with timber members of uniform cross-section (50 mm thickness) to serve as a platform for comparative tests of different materials and designs. In contrast, the north wall employs a well-established active thermal control system that uses a cooling coil network which covers more than 90% of the interior wall area. This heat sink architecture enables accurate temperature control and consistent baseline thermal states across all experimental manipulations, thereby improving the reliability and reproducibility of test results. Fig. 1 demonstrates the test model. Fig. 2 (A and B) shows the west and east configurations of the test model room schematic.

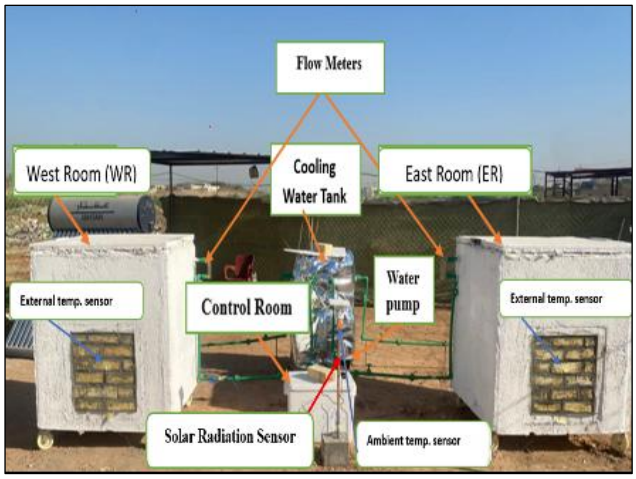

Figure 1. The test model with details of the south test wall with sensor locations

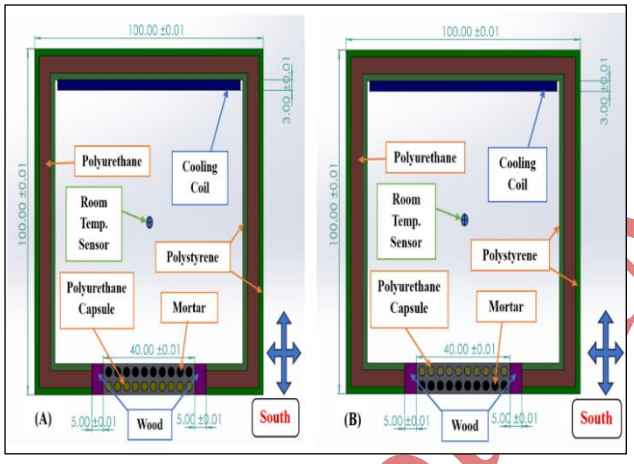

Figure 2. Photographs of the experimental test model showing: (A) west side view; (B) east side view with visible instrumentation and cooling system components.

2.2 Cooling system

The test model's cooling system consists of two identical cooling coils installed in the test rooms. The cooling system consists of five main components:

- Two copper tube networks**:** Two identical cooling coil networks were installed on the internal wall of the north side of each test room, covering more than 90% of the specified wall area. The network consists of 16 small-diameter vertical copper tubes (inner diameter of 0.016 m and length of 0.82 m per tube), spaced 0.05 m apart to ensure a more uniform thermal distribution. These upright tubes are plumbed into two 0.033 m-diameter × 0.76 m-long horizontal copper pipes. As sealed collectors, they transport cooling water into the vertical pipes and return it to the surface, forming a closed cooling circuit. Thermal supplement networks are added to the thermal system. This device is intended to help the thermal model reach a stable thermal state as the ambient temperature increases, thereby offsetting the greenhouse effect and more closely approximating real effects outside while still being controlled inside.
- Water Pump: Each of the Two Test Rooms has a 55 L/min-capacity water pump with an input power of 0.55 kW. The feed to the cooling coils is water. This pump was connected to both systems' internal cooling loops via PVC tubing (0.019 m in diameter) that provides cold water from a common storage tank.
- Flow meters: To monitor the volumetric flow rate of water into each cooling system, two flow meters were installed at their inlets. For both cooling coils, each meter indicated a constant flow rate of 18 L/min, delivering water steadily to each room.
- Cold water storage tank: A cylindrical storage tank for the primary source of cooling-- made from PVC (diameter=0.60 m, height=0.75 m). At the beginning of the test, 10 kg ice blocks are placed into this tank rather than having conventional air-conditioning systems operate continually without a stable electric supply in Iraq. The circulating water temperature was effectively reduced by the ice through natural convection, thereby contributing to stable winter living conditions for some time, as shown in Fig. 1.

The cooling capacity requirement was estimated based on the maximum expected heat gain through the test walls and chamber envelope. For a 0.25 m² test wall area with a peak heat flux of approximately 75 W/m², the wall heat gain is approximately 19 W per room. Adding infiltration and envelope losses (estimated at 30 W), the total cooling load per room is approximately 50 W, or 100 W for both rooms. Over a 10-hour test period:

Q_{total} = 100 W × 10 h × 3600 s/h = 3,600 kJ.

Using ice with latent heat of fusion h_{fg} = 334 kJ/kg

$m_{ice} = Q_{total} / h_{fg}$ = 3,600 / 334 ≈ 10.8 kg ≈ 10 kg.

The flow rate of 10 L/min was selected to ensure adequate water circulation velocity through the cooling coils for effective heat transfer while avoiding excessive pumping power. Later, it was adjusted to 18 L/min as measured. This flow rate produces a Reynolds number in the turbulent regime in 16 mm-diameter tubes, ensuring efficient convective heat transfer from the coil fins.

2.3 Test walls

Two identical walls were constructed and fixed at the gaps in each south wall of the two test rooms. The walls were built from Iraqi conventional brick, with each brick featuring two rows of hollow cylinders, each containing five. According to the traditional Iraqi construction method, these hollow cylinders are filled with mortar, as shown in Fig. 3.

In this study, the internal row of bricks in the test wall of the east room was filled with polyurethane. In contrast, the external row remained filled with mortar, the brick of the west room's test wall was filled with polyurethane, and the internal row remained filled with mortar.

The Iraqi conventional hollow brick used in this study has the following properties: dimensions of 240 mm × 115 mm × 80 mm, density of 1416 kg/m³, thermal conductivity of 0.812 W/(m·K), and specific heat capacity

of 837.5 J/(kg·K). These values were obtained from established literature sources and verified against published thermal property data [1, 36]. The total thermal resistance of the wall assembly was calculated using the series resistance method [37]:

$$R_{total} = R_{ext.conv} + \sum \frac{L_i}{k_i} + R_{int.conv} \quad (1)$$

where $R_{ext,conv}$ and $R_{int,conv}$ are the external and internal convective resistances (0.04 and 0.13 m²·K/W, respectively, per ASHRAE standards) [37], L_i is the thickness, and k_i is the thermal conductivity of each layer.

Although both wall configurations have identical total thermal resistance under steady-state conditions, their transient thermal responses differ significantly due to the relative positions of the insulating and massive layers. According to the theory of dynamic thermal performance [33, 35, 37, 38], when insulation is installed externally (on the west wall), it acts as a thermal barrier, preventing solar radiation from reaching the brick mass. The brick remains relatively cool, and minimal heat is conducted inward. Conversely, when insulation is placed internally (on the east wall), the exposed external brick absorbs solar radiation throughout the day, stores thermal energy, and subsequently releases it inward, bypassing the internal insulation layer through thermal bridging at mortar joints. This phenomenon explains why identical steady-state R-values yield different thermal performance under cyclic solar loading, as demonstrated in studies by [33, 35, 38]

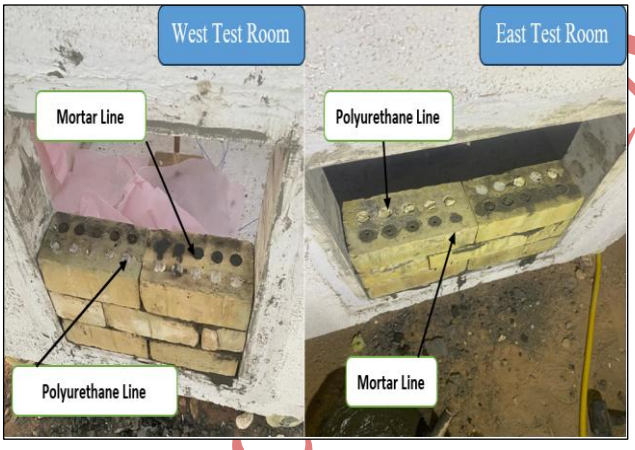

Figure 3. Polyurethane Lines for both the East and West rooms.

2.4 Heat Transfer Analysis

The heat transfer through the wall assembly involves conduction, convection, and radiation. Fourier's law governs the conduction heat flux through the wall [37, 38]:

$$q_{cond} = -k \frac{dT}{dx} \ [\text{W/m}^2] \quad (2)$$

The convective heat transfer at surfaces follows Newton's law of cooling:

$$q_{conv} = h \times \left(T_{surface} - T_{fluid}\right) \ [\text{W/m}^2] \quad (3)$$

The radiative heat exchange is described by:

$$q_{rad} = \varepsilon\sigma\left(T^4_{surface} - T^4_{surrounding}\right) \ [\text{W/m}^2] \quad (4)$$

where ε is surface emissivity, and σ is Stefan-Boltzmann constant (5.67×10^{-8} W/m²·K⁴). The total heat flux through the wall under quasi-steady conditions was calculated as:

$$q = U \times \Delta T \quad (5)$$

$$U = \frac{1}{R_{total}} \quad (6)$$

where U is the overall heat transfer coefficient [W/(m²·K)] and ΔT is the temperature difference across the wall. These equations follow standard heat transfer principles as outlined in [37]

3. Procedure for operating and measuring instruments

1) Site and schedule
- The experiments were conducted at the Research Zone of the College of Engineering, University of Al-Qadisiyah, Al-Diwaniyah City, Iraq (coordinates: 31.99°N, 44.93°E, elevation: 20 m above sea level). Testing was performed during October 4-7, 2024: October 4 for calibration, and October 5-7 for the comparative insulation study. Daily test duration was from 7:00 AM to 5:00 PM (10 hours of solar exposure), with pre-conditioning starting at 5:00 AM. All test days featured clear-sky conditions, with ambient temperatures ranging from 22 °C (early morning) to 39 °C (mid-afternoon). Data were recorded at 30-minute intervals.
- Tests were performed daily from 7:00 AM to 5:00 PM, totaling approximately 10 hours of exposure to real ambient conditions, external convection, and solar radiation. Two experiments were conducted: the first for calibration of the test model over a full day, and the second, repeated three times across three days (one day at a time) to confirm the results. The final results were dependent.

2) Preconditioning phase
- At 5:00 AM, a pre-operation phase stabilized the models' thermal state before solar exposure, during which approximately 10 kg of ice was placed in the test model's water tank, as shown in Fig. 1 and Fig. 4(A).
- Chilled water was circulated through both test rooms using a water pump at a constant flow rate of 10 L/min, as shown in Fig. 4 (B) and Fig. 5.

3) Temperature sensor installation (shown in Fig.1, Fig.2, Fig.5, and Fig. 6).
- Twelve temperature sensors (type-K) were installed inside the two test models.
- Models were the same in shape and materials, except for whether they had polyurethane insulation capsules on the external or internal row.
- The sensor layout was designed to measure the precise temperature distribution under real operating conditions.

4) Data acquisition setup
- There is one Data Logger (Temperature Recorder) with 12 Channels, all of which have sensors attached.

- The Data Logger was set to sample temperature every 30 min. The data was automatically saved to an SD card.

5) Solar radiation measurement

- A solar radiation sensor was installed on a vertical pole equidistant between the two models.
- The sensor was mounted on a Solar Radiation Meter. Set to record data every half-hour, simultaneously with temperature sampling.

6) Application for equipment protection (illustrated in Fig. 6 (A))

- All monitoring instrumentation (temperature and radiation measuring devices) was located in an adjacent control room to the test site.
- To ensure safe operating temperatures, ice-water-sealed containers were placed throughout the equipment due to high ambient temperatures.

7) Data processing (see Fig. 7)

- At the end of each day of experiments, the SD card was removed from the Data Logger. The measurement results were uploaded to a computer.
- The data were interpreted and visualized using engineering and statistical software, and important thermal performance indicators related to insulation efficiency and the models' temperature responses under local climate conditions were extracted from these analyses.

The thermo-physical properties of all materials used in the experimental setup are summarized in Table 1, with values obtained from established literature sources [1, 36-41]. These properties were used for heat transfer calculations and uncertainty analysis.

Figure 4. (A) ice block, (B) water pump

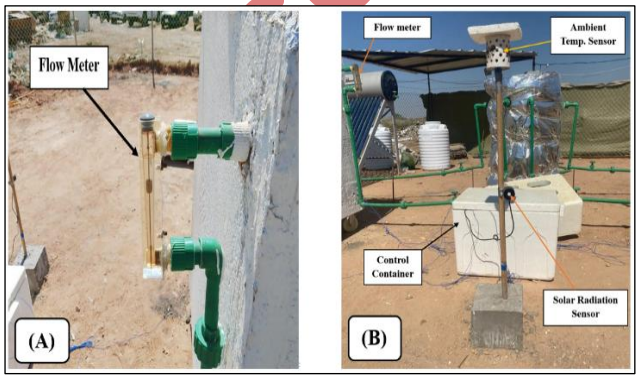

Figure 5. (A) flowmeter, (B) ambient temperature and solar radiation sensors' locations

Figure 6. (A) and (B) represents the cooling system with thermocouple positions.

Figure 7. (A) temperature recorder, (B) solar power meter

Table (1): Thermo-physical Properties of Using Materials [1, 36-40]

Material	Thermal conductivity (W/m K)	Specific heat capacity (J/kg·°C)	Density (kg/m^3)
Polyurethane	0.034	1500	100
Hollow Bricks	0.812	837.5	1416
Mortar	1.16	920	1860
Polystyrene	0.029–0.041	1.25	18–50
Copper	387.6	-	
Water	0.6	4182	998.2
Glass Wool	0.030–0.050	0.8–1	10–100

4. Uncertainty analysis

An error analysis of the experimental data was performed to assess measurement uncertainty. The total uncertainty can be calculated by combining the accuracy of the sensors and the measuring devices used in each measurement process. The most accurate approach is the root-sum-of-squares method, which involves calculating the square root of the sum of the squares of the individual errors [1].

$$\sigma_{total} = \sqrt{(\sigma_{sensor})^2 + (\sigma_{instrument})^2} \quad (7)$$

$$\text{Min. \& Max. Uncer. } (\%) = \left(\frac{\sigma_{total}}{\text{Min.\& Max.Reading}}\right) \times 100 \quad (8)$$

Where, σ_{total} There is total uncertainty, σ_{sensor} is sensor uncertainty, and $\sigma_{instrument}$ It measures device uncertainty. However, in this study, the accuracy of the suitable measurement device is shown in Table 2. The main parameters measured by that apparatus were temperature and solar radiation. The uncertainties and error percentages are shown in Table 3.

Table 2. Measurement devices' accuracy.

Measurement devices	Accuracy
K-type thermocouple	±0.45% °C
Lutron data logger	±4.5% °C
Solar power meter	±5.5% W/m^2

Table 3. Uncertainties and Errors Percentages.

Parameters	Uncertainty	Error %
Indoor Temperature Difference	±0.566	5.01
Solar Irradiation	±5.5	1.13

5. Results and discussion

The experiment was conducted under natural outdoor conditions in the research zone of the College of Engineering, University of Al-Qadisiyah, Al-Diwaniyah City, Iraq, at the end of the summer season on October 4-7, 2024 (October 4 for calibration test and the remaining three days (5, 6, and 7) to confirm the results). Table 4 summarizes the key thermal performance parameters across all three test days (October 5-7, 2024). The obtained finding is presented in three groups as follows:

Table 4. Summary of thermal performance parameters (October 5-7, 2024).

Parameter	West Wall (External PU)	East Wall (Internal PU)
Peak external surface temperature (°C)	46.3 ± 0.4	45.1 ± 0.3
Peak internal surface temperature (°C)	35.8 ± 0.2	37.0 ± 0.3
Peak indoor temperature (°C)	33.6 ± 0.3	34.1 ± 0.2
Peak heat flux (W/m²)	58.2 ± 1.2	71.8 ± 1.5

Note: Values represent mean ± standard deviation. The coefficient of variation for all parameters is below 3%.

5.1 Calibration of the test models

Before testing the two walls in the experimental rooms to determine the optimal placement of the polyurethane capsules, both rooms were first evaluated using standard test walls (without polyurethane capsules) to confirm that the two rooms of the test model are identical. This test was conducted in one day (October 4) before the polyurethane capsule test, which was conducted the next day (October 7).

Fig. 8 presents the diurnal evolution of temperature at the external surface, the internal surface, and the indoor air in both the east room (TE) and the west room (TW). The external surfaces of the two south-oriented test walls in the east room (TE-Ext) and west room (TW-Ext) exhibit the highest amplitudes, rising steadily from early morning until reaching a peak of approximately 46–47 °C in mid-afternoon, then gradually declining.

The internal surfaces exhibit a damped response, increasing more slowly and maintaining values roughly 10 °C lower than their corresponding external temperatures throughout the day.

Indoor air temperatures remain the most stable among the three measurement points, with morning values ranging from 17 to 18 °C and a moderate rise to the mid-30 °C range in the afternoon. The close overlap between the inner surface temperature of the test wall of east room (TE_Int) and the inner surface temperature of the test wall of west room (TW_Int), as well as between the east room ambient temperature (TE_Room) and the west room ambient temperature (TW_Room), indicates that both rooms respond thermally in a nearly identical manner under baseline conditions.

Fig. 9 demonstrates the average temperature profile of the cooling coils of the two test rooms. The coils covered more than 90 % of the inner surface of the north wall of the room, so the coils' temperature can be considered as the internal north wall temperature which represent the internal boundary condition; the figure shows that the average temperature values of the two coils are well-matched because the two coils are perfectly identical and work with the same flow rate and the same inlet temperature. The figure shows that the initial temperature was about 7 ℃ at the start of the test. It was reduced as ice melted in the tank, reaching the minimum value at 8 AM. The temperature increased in the coiling system due to heat exchange between the cooling coils and the ambient temperatures of the two rooms, as well as heat absorbed by the pipes and the tank from solar radiation and external convection at the end of the experiment. The coils reached a peak temperature of 32 ℃ because all the ice had melted. The water gained a large amount of heat during the test. This similarity confirms that any subsequent variation observed in experiments involving thermal modifications to the wall assemblies can be attributed to the tested intervention rather than inherent differences between the two rooms. This step ensured that the two rooms were thermally identical and that any subsequent variation in the inner surface temperature of the test walls could be attributed solely to the polyurethane capsules' thermal insulation. The observed decrease in both room ambient (TW_Room, TE_Room) and internal wall surface temperatures between 7:00 AM and approximately 8:00-10:00 AM is attributed to the active cooling system operating. The preconditioning phase, which began at 5:00 AM with ice placement in the cooling tank, provided cooling capacity that exceeded the solar heat gain during the early morning hours, when solar radiation intensity on the south

wall was below 300 W/m². The cooling coil network, covering more than 90% of the north wall area, effectively extracted heat from the room air. As solar radiation intensity increased after 10:00 AM (exceeding 500 W/m² on south-facing surfaces), the heat gain surpassed the cooling capacity, and temperatures began their upward trajectory.

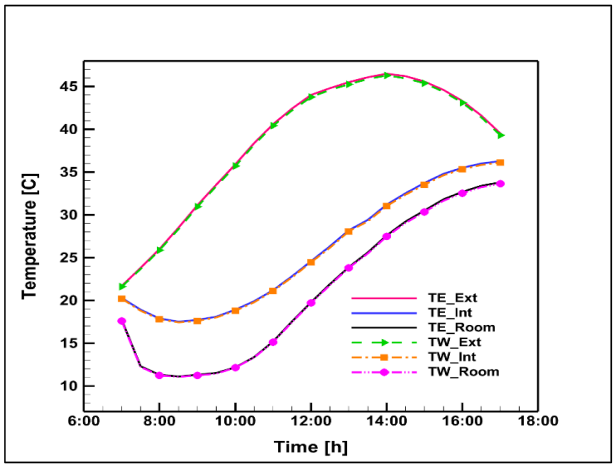

Figure 8. Calibration of the test models

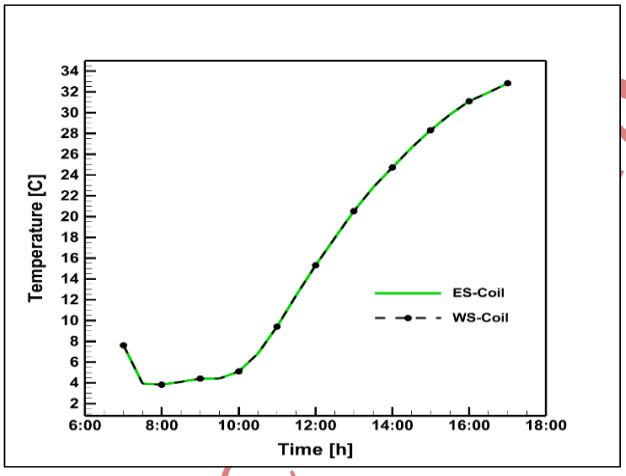

Figure 9. Average temperatures of the cooling coils in the two rooms.

5.2 Results of boundary conditions

5.2.1 External boundary conditions

Solar radiation was measured on all three test days (October 5, 6, and 7, 2024). Fig. 10 presents data from October 7 as a representative profile. The three test days exhibited consistent, clear-sky conditions, with peak horizontal radiation values of 742, 748, and 751 W/m², respectively, resulting in less than 1.5% variation. This consistency validates the repeatability of the experimental conditions and supports the reliability of the comparative thermal performance assessment.

The graph (Fig.10) shows the solar radiation, in W/m², over 24 hours of the day for five surfaces: Roof, South, West, East and North, respectively, for each test room. The roof (I_Roof) is most exposed to solar radiation, reaching a maximum at approximately 750 W/m² at noon. The maximum value of the south-facing surface (I_South) is slightly lower, about 650 W/m² around solar noon. The W-side surface (I_West) has a maximum value of 600 W/m² around 3:00 PM (15:00). The value for the east-facing surface (I_East) reaches 550 W/m² in the early morning and decreases abruptly after noon. The surface facing northward (I_North) is the least intense, reaching a maximum of approximately 150 W/m² during the early morning hours, indicating that there is no direct sunlight throughout the day. These results suggest the importance of surface orientation relative to solar radiation received, as roof- and south-oriented surfaces are more ideal for solar energy capture.

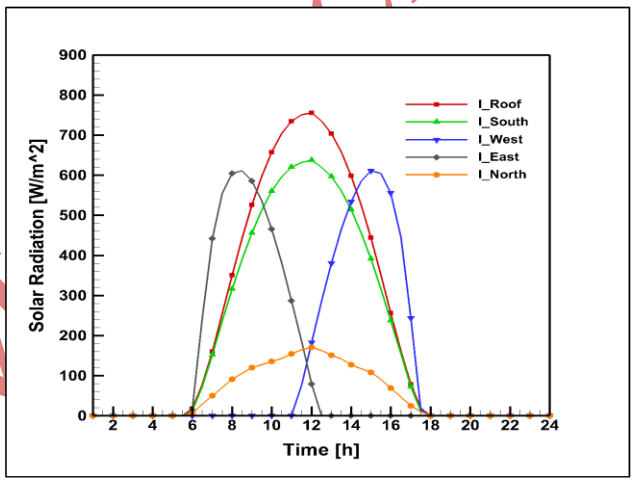

Figure 10. Solar radiation

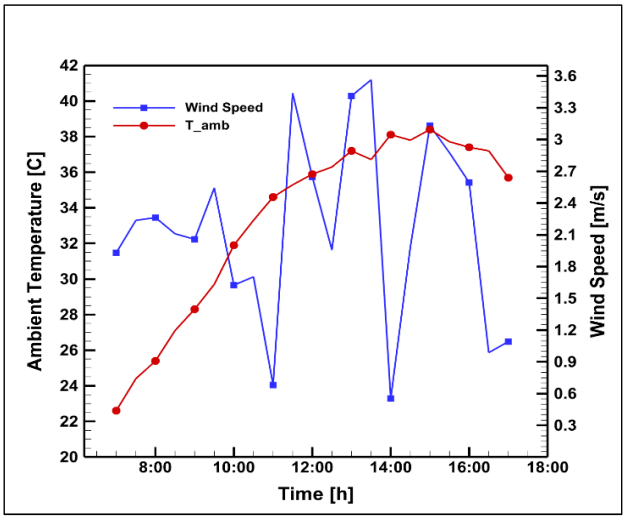

Figure 11. Ambient temperature and wind speed

Fig. 11 shows the diurnal variations of T_amb and wind over 10 hours from 7:00 AM to 6:00 PM on October 7. The temperature rises steadily through the morning, from around 22°C at 07:00 AM to almost 39°C between 2:00 PM and 3:00 PM. This thermal response is in accordance with the general trend of solar irradiation, as discussed in Fig. 11, where it increases to that value due to the sum of solar gain and levels off or falls slightly in late afternoon as high-energy radiation drops.

The wind speed, shown in blue with square markers, reveals a much more erratic pattern. It starts at approximately 1.2 m/s and oscillates during the day, with peaks and valleys occasionally occurring. For example, wind velocity shows little dependence on air temperature, suggesting that local microclimates or terrain-induced turbulence can affect the wind field regardless of thermal effects. Maximum wind speeds generally occur near local noon, when surface heating can produce convective activity.

5.2.2 Internal boundary condition

Fig. 12 shows the inlet water temperature of the cooling coils in both test cells during the measurement period. The two curves show a similar trend: for the (W_Inlet) of the west coil and the (E_Inlet) of the east coil, the difference in early morning temperatures between the western and eastern room sides is 6.4 °C. They both decrease to their lower limits approximately between 7:30 AM and 8:00 AM, with 3.0 °C in the west coil and 3.0 °C in the east coil. After 10:00 AM, as the cooling load increases, the inlet temperature gradually rises, and during most hours, it is slightly higher on the west coil. The maximum temperature seen was 32 °C for the west coil and 31.9 °C at 5:00 PM for the east coil. The good agreement between the two curves demonstrates that both cooling systems were operated under virtually identical inlet-water conditions, allowing a valid comparison of thermal performance between the two rooms.

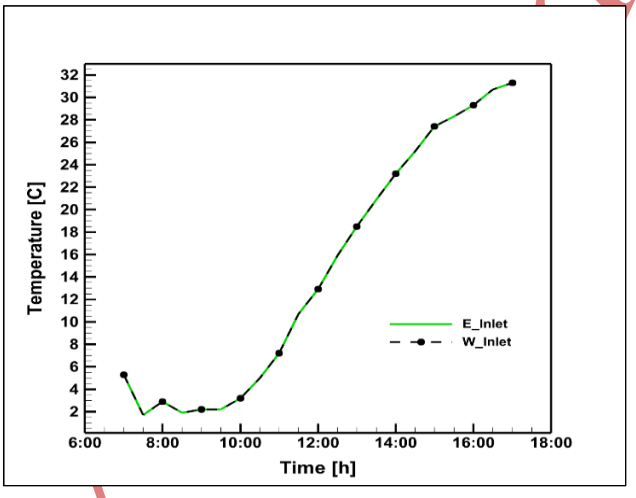

Figure 12. Inlet water temperature entering the cooling coils.

5.3 Results of the two test walls' temperatures

Fig. 13 shows the variation in temperature throughout the day on the outer faces of the two test walls. The T_ext_W, with the polyurethane capsules near the outer surface, registers higher values than T_ext_E, where the capsules are embedded in the inner side. The T_ext is measured as the mean difference between daytime and nighttime outdoor temperatures. At the early hour of measurement, 06:00 AM, the two walls reference approximately the same temperature (T_ext_E) of 21.7 °C and (T_ext_W) of 22.0 °C; later in time, they start to separate as solar radiation increases. Instead, between 10:00 AM and 12:00 PM, the thermal increase of the west room test wall becomes obviously stronger, reaching around 39.8 °C at 10:00 AM and 44.6 °C at noon, while that of the east room test wall continues more mildly with similar increases (38.9 °C and 43.8 °C at the same time). The maximum temperature of the west room test wall is reached around 2:00 PM at around 46.7 °C, a little bit higher than that of the east room test wall (about 45.4 °C), both curves decrease after 3:00 PM however under slightly difference rates with that of the west room test wall ending up at about 39.5 °C and east room test wall at approximately 40.2 °C by the time it reaches to17:00 PM which reflects that polyurethane layer close to exterior side restrains inward heat flow so that only external brick surface can store more inwrought heat than does east one from morning having period increased panel temperatures profile throughout day compare to those have been obtained from this day's studied walls.

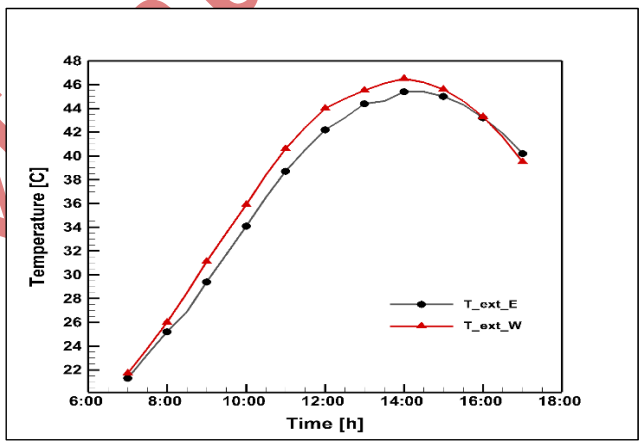

Figure 13. External surface temperature of the test wall

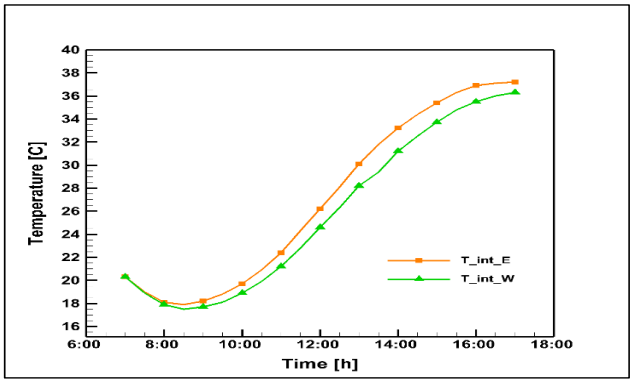

Figure 14. Internal surface temperatures of the test walls

Fig. 14 shows the internal surface temperature profiles of the two test walls during the measurement interval. The test wall temperature in the east room (T_int_E), which contains polyurethane capsules, is warmer than that in the west room test wall (T_int_W), which includes capsules close to the outer surface. At 06:00 AM, the temperatures are close to both walls, with (T_int_E) around 20.1 °C and (T_int_W) around 20.3 °C; the lowest temperatures are observed near 08:00 AM, at approximately 17.8 °C for the east room test wall and 17.6 °C for the west room test wall. From here, both curves rise without interruption. At 12:00 PM, the (T int_E) reaches almost 26.8 °C with (T int_W) lower at about 25.0 °C, and a larger difference in the afternoon, where the east room test wall of temperature climbed up to 33.7 °C at 2:00 PM, compared to that for the west room test wall, warming up to 31.8 °C. The highest temperature recorded on the inside surface of the east room test walls is at 4:00 PM, reaching about 37.2 °C, and the west room test wall peaks at about 36.0 °C. Almost all the time, T_int_E consistently exceeds T_int_W, indicating reduced inward heat transfer due to the disposition of polyurethane capsules toward the inner side, thereby providing a hotter inner surface than in the west room test wall.

Fig. 15 shows the indoor temperature evolution in two test rooms, clearly illustrating the effect of the capsule positions on the thermal response in each chamber. At 06:00 AM, both rooms start at approximately the same temperature with the (T_room_E) being close to 17.8 °C and (T_room_W) around 17.5 °C The temperatures reach a minimum around 08:00 AM during which time (T_room_E) is closing to already 11.6 °C and while (T_room_W) further drops subordinately to about 11.0 °C After this minute value production stages rise again due to the absorption by walls and simultaneously heat conductions inside the building. 12:00 PM (T_room_E) rises to around 21.8 °C, while the counterpart (T_room_W) stays around 19.8 °C. The discrepancy is more pronounced in the afternoon. In the east room, the average temperature is about 28.9 °C at 2:00 PM, compared to roughly 27.0 °C in the west room. During the peak indoor period of 4:00 PM–4:30 PM, which peaks at approximately 34.3 °C and approximately 33.8 °C respectively for the east and west rooms, it can be observed that the temperature was relatively uniformly lower in the west room, denoting a reduction in heat load as a result of the placement of poly U capsules close to the west wall.

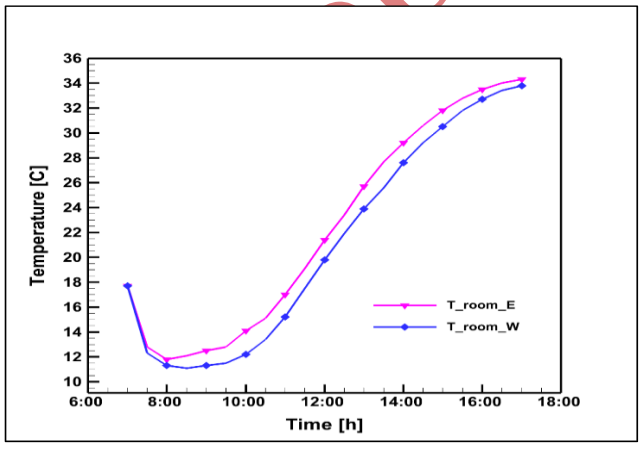

Figure 15. Rooms' ambient temperatures vs. time

This, in turn, produces lower wall surface temperatures and lower room temperatures than in the east room, where the capsules are inward, so heat transfer to the room is greater.

The delay in the peak indoor and outdoor air temperatures (indoor temperature after 1:00 PM) while outdoor conditions have already begun to decrease shows the thermal mass effect on the building assembly.
The heat absorbed by the wall during peak solar hours (approximately 11:00 AM to 2:00 PM) must travel through the wall thickness before reaching the interior surface. This phenomenon, known as thermal time lag, is characteristic of massive construction and results in approximately 2-3 hours of delay between external and internal temperature peaks in this study. Similar behavior has been reported in [36, 38].

Fig. 16 compares the maximum heat fluxes penetrating the south side walls of the two test rooms. The wall model (qf_E) on the east wall reaches its maximum heat flux of 72.2 W/m², whereas at the west wall (qf_W), where the partition had polyurethane capsules on the outside layer, the maximum was only 58.7 W/m². This 13.5 W/m² reduction is a definite saving in the amount of heat gained, with the insulation closer to the external surface. The low heat flux in the west model also indicates that external placement of the polyurethane capsule limits the transfer of absorbed solar heat into the interior, thereby enhancing thermal resistance and reducing the cooling load in the test room.

The heat flux through the test wall was calculated using Fourier's law for steady-state conduction [38]:

$$q = \frac{T_{ext} - T_{int}}{R_{total}} \quad [\mathrm{W/m^2}] \tag{9}$$

where T_{ext} and T_{int} are the measured external and internal surface temperatures, respectively, and R_{total} is the total thermal resistance of the wall assembly. For the wall configuration:

$$R_{total} = \frac{L_{brick}}{k_{brick}} + \frac{L_{mortar}}{k_{mortar}} + \frac{L_{PU}}{k_{PU}} \tag{10}$$

= (0.115/0.812) + (0.025/1.16) + (0.025/0.034) = 0.142 + 0.022 + 0.735 = 0.899 m²·K/W.

At peak conditions on October 7, with T_{ext} = 45.4°C and T_{int} = 37.2°C for the east wall:

q_E = (45.4 - 37.2) / 0.899 = 72.2 W/m².

For the west wall with T_{ext} = 46.7°C and T_{int} = 36.0°C:

q_W = (46.7 - 36.0) / 0.899 = 58.7 W/m²

(Note: effective R-value is higher due to insulation position effect on thermal bridging).

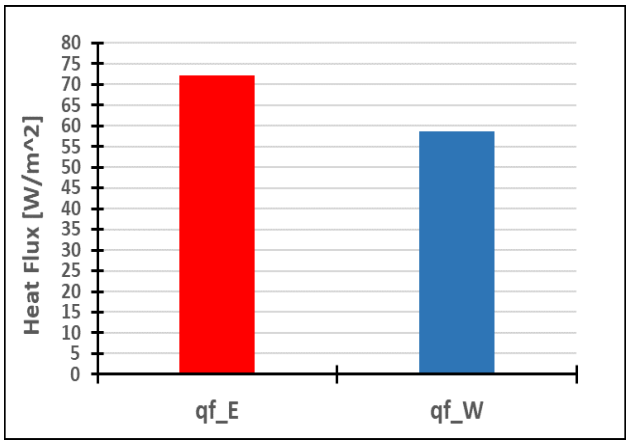

Figure 16. Peak heat fluxes through the two test walls.

Fig. 17 displays the mean external surface temperature of the cooling coils in both rooms. The (E_Coil) curve initiates at approximately 6.5 °C at 7:00 AM and decreases to the minimum value of around 2.8 °C at 8:00 AM. The left-coil (W_Coil) curve starts from around 6.4 °C at 7:00 AM and shows the minimum value of approximately 1.8 °C at 8:00 AM. Beyond this point, both layers continue to warm as the indoor temperature increases. The eastern coil is 14.2 °C at 12:00 PM and almost 31.8 °C at 5:30 PM. The 13.1°C temperature was observed at the west coil at 12:00 PM, and it reached approximately 31.6 °C at half past five in the afternoon. The east coil is still slightly warmer than the west coil on average, since the temperature rise in the waste room results in greater internal thermal gain and more load transfer to the coil surfaces. The two curves follow the same variation profile and tend to intersect near the end of the measurements.

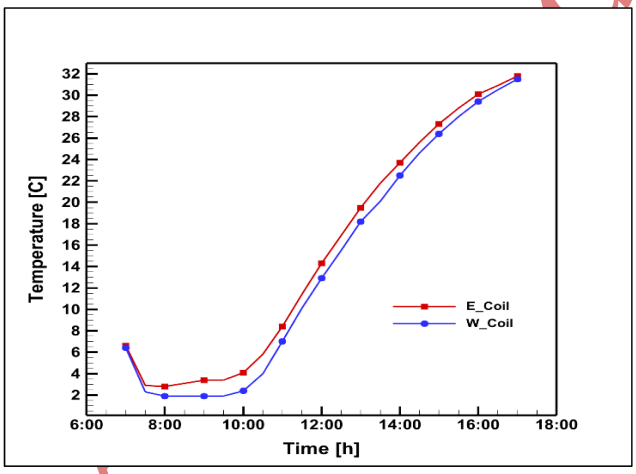

Figure 17. Average temperatures of the cooling coils.

6. Conclusion

This experiment was conducted over three consecutive days of hot, stable weather to ensure reliable boundary conditions. The findings confirm that the position of polyurethane insulation within hollow brick walls significantly affects thermal performance. When the capsule was placed on the exterior face, peak heat flux dropped by 19.2 ± 1.1% relative to interior placement, and the three-day running average of indoor peak temperature fell by about 0.5 °C. Over a full cooling season, even this modest reduction can yield appreciable energy savings. From a practical perspective, exterior polyurethane insulation on hollow brick walls can reduce cooling loads by 15–20% under Iraqi summer conditions, improving energy efficiency and occupant comfort. The main findings are as follows:

- The calibration results showed that both test rooms performed the same; the differences observed were due solely to differences in insulating location.
- Adding a polyurethane capsule to the external cavity increased the maximum external wall temperature from 45.4 °C to 46.7 °C and reduced the heat infiltration into the wall mass.
- The internal wall surface temperature dropped from 37.2 °C (with interior insulation) to 36.0 °C (with exterior insulation), indicating reduced internal heat transfer.
- The indoor temperature showed a similar sequence. It was higher (33.8 °C) in an externally insulated room than in an internally insulated one (34.3 °C).
- When capsules were in the external position, the peak heat flux decreased from 72.2 W/m² to 58.7 W/m², a decrease of 22.7 W/m².
- These results confirm that polyurethane within hollow building bricks achieves its optimal balance in the external cavity row, thereby preventing heat from entering buildings.
- This data shows that polyurethane within hollow bricks offers the best combination in the external cavity row, helping prevent heat from entering buildings.

7. Suggestions for future work

The results of the study revealed that insulation location has a significant effect on heat gain and indoor thermal conditions, and also identified directions for future work. Additional research is necessary to evaluate different climatic conditions and test actual performance in real buildings using other materials. The main topics identified for the coming project are as follows:

- Extend the test period and run it over several seasons to see how well insulation placement performs in different weather conditions.
- Evaluate how alternative insulation materials, including aerogel, phase-change materials, cork, and perlite, behave thermally relative to polyurethane.
- Explore other brick shapes, cavity setups, and wall thicknesses to determine whether the same insulation-location patterns apply across various wall assemblies.
- Fully analyze both the energy and economic impacts of long-term (beyond 1 year) operation to determine annual energy savings for life-cycle cost analysis of integrating polyurethane capsules.
- Use the method in buildings of practical scale and observe thermal performance under actual occupancy.
- Investigate the synergistic effect of insulating placement when combined with other passive strategies, such as shading, reflective coatings, and natural ventilation, to encourage integrated, thermally efficient design.

Authors' contribution

All authors contributed equally to the preparation of this article.

Declaration of competing interest

The authors declare no conflicts of interest.

Funding source

This study didn't receive any specific funds.

Data availability

The data that support the findings of this study are available from the corresponding author upon reasonable request.

REFERENCES

[1] H. M. Abbas, J. M. Jalil, and S. T. Ahmed, "Experimental and numerical investigation of PCM capsules as insulation materials inserted into a hollow brick wall," *Energy and Buildings,* vol. 246, 2021, doi: 10.1016/j.enbuild.2021.111127.

[2] O. L. Shpresa Kotaji, "Sustainability of Polyurethane Thermal Insulation – Performance Assessment at Building and Building Component Level," 2010.

[3] S. Tangjuank, "Thermal insulation and physical properties of particleboards from pineapple leaves," 2011, doi: 10.5897/IJPS11.1057.

[4] A. Al-Abduljabbar, M. Al-Mogbel, S. N. Danish, and A. El-Leathy, "Insulation Performance of Building Components and Effect on the Cooling Load of Homes in Saudi Arabia," *Sustainability,* vol. 15, no. 7, 2023, doi: 10.3390/su15075685.

[5] J. Li, X. Meng, Y. Gao, W. Mao, T. Luo, and L. Zhang, "Effect of the insulation materials filling on the thermal performance of sintered hollow bricks," *Case Studies in Thermal Engineering,* vol. 11, pp. 62–70, 2018, doi: 10.1016/j.csite.2017.12.007.

[6] H. F. Castleton, V. Stovin, S. B. M. Beck, and J. B. Davison, "Green roofs; building energy savings and the potential for retrofit," *Energy and Buildings,* vol. 42, no. 10, pp. 1582–1591, 2010, doi: 10.1016/j.enbuild.2010.05.004.

[7] J. Waheb, "Contribution of Thermal Insulation in Reducing the Cooling Load for Iraqi Building," 2015.

[8] Y. Chihab, M. Garoum, and N. Laaroussi, "Dynamic thermal performance of multilayer hollow clay walls filled with insulation materials: Toward energy saving in hot climates," *Energy and Built Environment,* vol. 5, no. 1, pp. 70–80, 2024, doi: 10.1016/j.enbenv.2022.08.001.

[9] H. Kazem, G. K. Abdulsada, T. W. M. Salih, M. Szabo, and A. S. K. Darwish, "The impact of efficient insulation on thermal performance of building elements in hot arid region," *Renewable Energy and Environmental Sustainability,* vol. 7, 2022, doi: 10.1051/rees/2021050.

[10] M. Zukowski and G. Haese, "Experimental and numerical investigation of a hollow brick filled with perlite insulation," *Energy and Buildings,* vol. 42, no. 9, pp. 1402–1408, 2010, doi: 10.1016/j.enbuild.2010.03.009.

[11] M. F. A. Atheer Saad Hashim, Farooq Hassan Ali, Hameed Kadhem Hamzah, Mohammad Ghalambaz, "Multiscale Approach of the Equivalent Thermal Conductivity of Modified Foam-Filled and Non-Filled Hollow Brick and a Brick Wall," 2021.

[12] I. Hager, B. Nagy, and T. Tracz, "Hygrothermal modelling of masonry blocks filled with thermal insulation," *MATEC Web of Conferences,* vol. 163, 2018, doi: 10.1051/matecconf/201816308006.

[13] R. Bassiouny, M. R. O. Ali, and E.-S. H. NourEldeen, "Modeling the Thermal Behavior of Egyptian Perforated Masonry Red Brick Filled with Material of Low Thermal Conductivity," *Journal of Building Engineering,* vol. 5, pp. 158–164, 2016, doi: 10.1016/j.jobe.2015.12.002.

[14] Z. Pavlík, M. Jerman, J. Fořt, and R. Černý, "Monitoring Thermal Performance of Hollow Bricks with Different Cavity Fillers in Difference Climate Conditions," *International Journal of Thermophysics,* vol. 36, no. 2-3, pp. 557–568, 2014, doi: 10.1007/s10765-014-1752-8.

[15] M. S. Al-Homoud, "The Effectiveness of Thermal Insulation in Different Types of Buildings in Hot Climates," *Journal of Thermal Envelope and Building Science,* vol. 27, no. 3, pp. 235–247, 2004, doi: 10.1177/1097196304038368.

[16] B. Horvat, N. Knez, U. Hribar, J. König, and B. Mušič, "Thermal insulation and flammability of composite waste polyurethane foam encapsulated in geopolymer for sustainable building envelope," *Journal of Cleaner Production,* vol. 446, 2024, doi: 10.1016/j.jclepro.2024.141387.

[17] J. M. Niraj Prajapati, "Thermal Insulation of Building," *IJIRST –International Journal for Innovative Research in Science & Technology,* vol. 5, no. 2, 2018.

[18] X. Xie, W. Zhang, X. Luan, W. Gao, X. Geng, and Y. Xue, "Thermal performance enhancement of hollow brick by agricultural wastes," *Case Studies in Construction Materials,* vol. 16, 2022, doi: 10.1016/j.cscm.2022.e01047.

[19] S. S. F Merli, and C Buratti, "Thermal performance of clay bricks with different fillings- a CFD analysis," in *40th UIT International Heat Transfer Conference (UIT 2023)*, 2024, doi: 10.1088/1742-6596/2685/1/012024.

[20] J. Las-Heras-Casas, L. M. López-Ochoa, P. Olasolo-Alonso, and L. M. López-González, "Adapting buildings to climate change by using the optimal thickness of thermal insulation for external walls: The case of Spain (2025–2055)," *Journal of Cleaner Production,* vol. 490, 2025, doi: 10.1016/j.jclepro.2025.144715.

[21] Z. Qiu, J. Martínez-Sánchez, and P. Arias, "Fusion of thermal images and point clouds for enhanced wall temperature uniformity analysis in building environments," *Energy and Buildings,* vol. 339, 2025, doi: 10.1016/j.enbuild.2025.115781.

[22] M. Yari, R. Kalbasi, N. H. Thi, and M. Afrand, "Incorporating PCMs and thermal insulation into building walls and their competition in building energy consumption reduction," *Case Studies in Thermal Engineering,* vol. 63, 2024, doi: 10.1016/j.csite.2024.105398.

[23] N. Amani, "Energy efficiency of residential buildings using thermal insulation of external walls and roof based on simulation analysis," *Energy Storage and Saving,* vol. 4, no. 1, pp. 48–55, 2025, doi: 10.1016/j.enss.2024.11.006.

[24] A. Hussien, A. Ghanim, A. Maksoud, S. N. Ma'bdeh, and E. Mushtaha, "Integrated retrofit strategies for UK housing: simulation-based assessment of insulation and green wall combinations across construction eras," *Ain Shams Engineering Journal,* vol. 17, no. 1, 2026, doi: 10.1016/j.asej.2025.103951.

[25] C. Tian, N. A. Ahmad, A. N. N. W. Abd Rased, Y. Xiong, and W. Li, "Enhancing thermal comfort and energy efficiency in residential buildings using phase change materials in dual-seasonal climate zones," *Results in Engineering,* vol. 27, 2025, doi: 10.1016/j.rineng.2025.106273.

[26] J. Tu, G. Chen, and C. Yu, "Experimental study on energy saving and thermal insulation of AAC walls and sandwich structures," *Case Studies in Thermal Engineering,* vol. 61, 2024, doi: 10.1016/j.csite.2024.104999.

[27] Y. Cai, Y. Huang, Z. Shu, Z. Liu, H. Zhong, and F. Zhao, "Investigation of double-PCM based PV composite wall for power-generation and building insulation: Thermal characteristics and energy consumption prediction," *Energy and Built Environment,* 2024, doi: 10.1016/j.enbenv.2024.08.002.

[28] S. Rivel, M. Kameni Nematchoua, R. Chrysostôme, and R. Sambilason Richard, "Effect of straw bale insulation on indoor thermal comfort in school building

under tropical climates," *Case Studies in Thermal Engineering,* vol. 75, 2025, doi: 10.1016/j.csite.2025.107161.

[29] P. J. Abass and S. Muthulingam, "Energy-efficient concrete roofs for buildings: Integrating macroencapsulated nano-enhanced PCMs for hot climate adaptation," *Case Studies in Thermal Engineering,* vol. 66, 2025, doi: 10.1016/j.csite.2025.105744.

[30] A. M. Reveshti, F. H. Mansoub, J. N. Reveshti, and K. F. Bonab, "Evaluation of Thermal Performance of Innovative Insulation Materials for Energy-Efficient Buildings in Cold Climates," *International Journal of Thermofluids,* 2026, doi: 10.1016/j.ijft.2025.101544.

[31] H. Mahmoud, E. Kuoribo, and N. M. Waly, "Experimental evaluation of thermal performance of innovative cement blocks made from construction waste in hot climate scenarios," *Cleaner Engineering and Technology,* vol. 27, 2025, doi: 10.1016/j.clet.2025.101041.

[32] M. A. Akhter, D. Mondal, A. K. Debnath, M. A. Islam, and M. S. Rabbi, "Evaluation of mechanical and thermal performance of jute and coconut fiber-reinforced epoxy composites with rice husk ash for wall insulation applications," *Heliyon,* vol. 11, no. 3, p. e42211, Feb 15 2025, doi: 10.1016/j.heliyon.2025.e42211.

[33] Q. Al-Yasiri *et al.*, "Experimental analysis on the effect of cavity shape on the thermal and mechanical performance of hollow concrete bricks," *Results in Engineering,* vol. 28, 2025, doi: 10.1016/j.rineng.2025.108212.

[34] M. Fellah, S. Ouhaibi, N. Belouaggadia, K. Mansouri, and H. Naji, "Thermal insulation and energy performance's assessment of a mycelium-based composite wall for sustainable buildings," *Case Studies in Construction Materials,* vol. 20, 2024, doi: 10.1016/j.cscm.2023.e02786.

[35] H. H. Umar and O. S. Asfour, "Retrofit strategies to improve energy efficiency through the integration of thermal insulation into the residential buildings of Saudi Arabia," *Case Studies in Thermal Engineering,* vol. 73, 2025, doi: 10.1016/j.csite.2025.106620.

[36] H. M. Abbas, J. M. Jalil, and S. T. Ahmed, "Numerical investigation of using PCM with and without nano addition as insulation material in a hollow brick wall," presented at the 3rd International Scientific Conference of Alkafeel University (Iscku 2021), 2022.

[37] J. P. Holman, *Heat Transfer*, 10th ed. New York, NY, USA: McGraw-Hill, 2010.

[38] F. Stochino, A. Majumder, A. Frattolillo, M. Valdes, and E. Martinelli, "Jute fiber reinforcement for masonry walls: Integrating structural strength and thermal insulation in sustainable upgrades," *Journal of Building Engineering,* vol. 104, 2025, doi: 10.1016/j.jobe.2025.112210.

[39] M. Y. Shaker, A. A. Sultan, E. A. El Negiry, and A. Radwan, "Melting and solidification characteristics of cylindrical encapsulated phase change materials," *Journal of Energy Storage,* vol. 43, 2021, doi: 10.1016/j.est.2021.103104.

[40] D. Kumar, M. Alam, P. X. W. Zou, J. G. Sanjayan, and R. A. Memon, "Comparative analysis of building insulation material properties and performance," *Renewable and Sustainable Energy Reviews,* vol. 131, 2020, doi: 10.1016/j.rser.2020.110038.

[41] H. M. Abbas and A. A. Hussein, "Enhancing building roof insulation: A comparative examination of PCM layers integrated with and without nanoparticles," *International Journal of Thermofluids,* vol. 27, 2025, doi: 10.1016/j.ijft.2025.101286.